DE GRUYTER Green Processing and Synthesis 2023; 12: 20230058

Research Article

Haiyang Liu[#], Zhe Wang[#], Heng Zhang, Lixia Jin*, and Yuehui Zhao

Photocatalytic research performance of zinc oxide/graphite phase carbon nitride catalyst and its application in environment

https://doi.org/10.1515/gps-2023-0058
received April 03, 2023; accepted May 23, 2023

Abstract: In this article, ZnO quantum dots (QDs)-g-C_3N_4 complexes were prepared by a combined sol–gel method and ultrasound-assisted chemical method, and ZnO-g-C_3N_4 composites with different doping ratios were also prepared for photocatalytic degradation of dye wastewater. The composites were characterized by scanning electron microscopy, transmission electron microscopy, X-ray diffractometry, Fourier transform infrared, X-ray photoelectron spectroscopy, diffuse reflectance spectroscopy, and photoluminescence. The photocatalytic performance of the best ZnO QDs-g-C_3N_4 complexes with different g-C_3N_4 doping amounts was investigated, and the kinetics of their photocatalytic reactions were analyzed, and it was found that the best effect of ZnO-g-C_3N_4 10% could reach 89.08% and ZnO QDs-g-C_3N_4 could reach 91.53%. It was also demonstrated that ZnO-g-C_3N_4 10%, ZnO QDs-g-C_3N_4 cyclic stability is better, and the reaction mechanism of ZnO QDs-g-C_3N_4 was investigated. It can be used for the degradation of dyes in environmental wastewater and the removal of harmful substances from the natural environment.

Keywords: ZnO QDs, ZnO QDs-g-C_3N_4, photocatalytic performance, antibiotic drug degradation

1 Introduction

Rapid economic development from the past century to this century and the use of drugs and chemicals in agriculture have made water pollution more and more serious [1]. The deterioration of water quality in rivers and lakes and the scarcity of freshwater resources have seriously threatened the health of the water environment [2]. Especially in the era of rapid industrial development, printing and dyeing wastewater treatment has been a key issue. Dye wastewater with large amount, high organic content and high chroma is widely recognized as intractable industrial wastewater [3–6]. To solve these problems, numerous researchers have used various methods to treat dye wastewater [7].

Among the many water pollution treatment options that have been developed, photocatalysis is an effective method for solving water pollution problems because of its low operating costs, its ability to completely mineralize pollutants, and its ability to degrade organic pollutants to less toxic or non-toxic components [8]. Photocatalysis can use solar energy to degrade pollutants by exciting electron transfer in semiconductor photocatalysts [9]. The most important factor in this technology is the photocatalyst, which converts solar energy into chemical energy that destroys the pollutant. Currently, metals, metal oxides, nonmetals, semiconductors, metal–organic frameworks, and other materials have been extensively studied for the degradation of dye molecules in wastewater [10–12].

As a representative of photocatalytic materials, zinc oxide (ZnO) stands out in water treatment because of its unique attributes, such as low price, good stability, and obvious surface and interface effects [13–15]. However, ZnO photocatalyst itself also has some defects: its own light absorption capacity is very poor and electron-hole pair separation rate is very low [16–19]. Therefore, it has become a hot topic of research to improve the degradation efficiency under visible light through research on its own modification: doping modification, crystal appearance control, thin film loading, composite of different materials, etc. [20–23]. Also known as semiconductor nanoparticles or semiconductor nanocrystals, quantum dots (QDs) have a size-dependent electronic structure and excellent optoelectronic properties.

QDs have been regarded as a new generation of fluorescent biomarker probes that can replace traditional fluorescent

---

[#] These authors contributed equally to this work.

*** Corresponding author: Lixia Jin,** Heilongjiang University of Chinese Medicine, Harbin, Heilongjiang, China, e-mail: jinlixia1980@126.com
Haiyang Liu, Zhe Wang, Heng Zhang: Heilongjiang University of Chinese Medicine, Harbin, Heilongjiang, China
Yuehui Zhao: Inspection and Testing Center, Jiamusi, China

organic molecules by researchers worldwide and have been widely used in various disciplines such as cell labeling [24,25], nano-drug delivery [26–29], and biosensors [30]. The main methods commonly used for the synthesis of ZnO QDs are hydrothermal method [31], sol–gel method [32], and microemulsion method [33].

The advantages of g-C_3N_4, such as high stability of physicochemical properties, diverse structures, simple preparation, and abundant and cheap preparation materials, make it widely used in photocatalytic carbon dioxide conversion [34–38], photocatalytic pollutant treatment [39–41], photocatalytic organic synthesis [42–44], and especially in photocatalytic decomposition of aquatic hydrogen.

Rhodamine B (RhB) is one of the main pollutants in dye wastewater. RhB is a bright-red synthetic onion quinone dye. Because of its bright color, it is widely used in dyeing and textile industry.

Commonly used water treatment methods have high treatment costs, low removal rate, secondary pollution, and other disadvantages, so it needs a water treatment technology with high efficiency, environmental protection, complete reaction, and no secondary pollution. Semiconductor photocatalysis technology has thus emerged. It is favoured by researchers in environmental wastewater treatment due to its conditions of high efficiency, non-pollution, low energy consumption, simple operation and easy control. It can also directly convert organic matter in water into non-toxic materials without causing secondary pollution [45–48].

Waseem et al. [49] greatly improved the degradation rate by doping neodymium and erbium on ZnO, where the neodymium-doped ZnO was essentially completely degraded for methylene blue within 10 min. Suwiwat et al. [50] used highly mesoporous carbon-ZnO nanocomposites and found that the adsorption of methylene blue and Congo red were 399 and 410 mg g^{-1}, respectively, and the synergistic effect of adsorption and photocatalytic degradation resulted in a maximum removal of methylene blue of 614 mg g^{-1} and Congo red of 2,628 mg g^{-1}. Huang et al. [51] prepared thin layers of porous amino-rich g-C_3N_4 by a precursor modification strategy using different acid-reformed dicyandiamide and applied them to the degradation of RhB.

In this article, ZnO-g-C_3N_4, ZnO QDs-g-C_3N_4 complexes with different doping ratios were synthesized, and a series of characterizations were performed to demonstrate their successful preparation. The photocatalytic degradation experiments were carried out using RhB solution as the simulated dye wastewater in the degradation experiments under visible light. The stability of the catalyst was investigated after five cycles using catalyst cycling stability experiments. The principle of photocatalytic degradation of ZnO QDs and its complexes was investigated using free radical capture experiments.

2 Material preparation

2.1 Preparation of ZnO-g-C_3N_4

One gram of ZnO was added to a beaker containing 60 mL of anhydrous ethanol, and the corresponding mass of g-C_3N_4 weighed in different ratios was added to the beaker and sonicated for 1 h. It was poured into the hydrothermal reactor and put into the high temperature drying oven at 140°C for 10 h. The purpose of fully combining the two powders under high temperature and pressure was achieved. The material was removed and centrifuged, the supernatant was poured off, and the remaining powder was placed in a vacuum drying oven at 60°C for 24 h to dry the sample sufficiently. Then the samples were put into a high temperature drying oven at 200°C and kept for 120 min, which can improve the crystallinity and remove the water from the photocatalyst at the same time. The products were labeled as ZC-3, ZC-5, ZC-7, ZC-10, and ZC-20 by adding g-C3N4 with different mass fractions of 3%, 5%, 7%, 10%, and 20%, respectively.

2.2 Preparation method of ZnO QDs-g-C_3N_4

One gram of ZnO QDs is weighed and added into a beaker containing 60 mL of anhydrous ethanol; then 0.01 g of g-C_3N_4 is added into the beaker and ultrasonication is performed for 1 h so that the mixed solution can be fully mixed. After the ultrasound is finished, the material in the beaker is poured into the hydrothermal reaction kettle and put into the high-temperature drying oven. The temperature of the high-temperature drying oven is set at 140°C and the time is set at 10 h, to achieve the purpose of fully combining the two powders under high temperature and high pressure.

The material is taken out and centrifuged. The supernatant of the centrifuged material is poured out and the remaining powder was put into a vacuum drying oven at 60°C for 24 h to dry the sample. To improve the crystallinity of the samples, the samples were then placed in a high-temperature drying oven set at 200°C for 120 min. At the same time, the water in the photocatalyst was removed and the product was labeled ZC QDs-10.

3 Results and discussion

3.1 Effect of different pH solutions on the degradation performance of RhB

A measure of 0.02 g of photocatalyst ZnO-g-C_3N_4 10% composite was taken, and 50 mL of 10 mg·L^{-1} of RhB solution with pH values of 1, 3, 5, 7, and 11 were prepared. The effect of pH of the solution on the degradation performance was discussed by dark reaction for 60 min and light reaction for 6 h at room temperature. The experimental results are shown in Figure 1.

As can be seen from Figure 1, the degradation of catalyst is relatively good when the pH value is in the acidic range. When pH = 3, its degradation rate reaches the maximum, about 91%. The reason for this phenomenon is that the OH^- or H^+ added to the solution changes the charge characteristics and interface properties of the surface of the photocatalyst of ZnO-g-C_3N_4 10% composite material, as well as the existence form of degradation substances, which further affects the catalytic activity of the photocatalyst. When there is a large amount of OH^- in the solution, the catalyst itself is negatively charged, while the analog dye RhB is positively charged. At this time, it will trap the resulting photogenic holes, thus reducing the hydroxyl radical. Therefore, in alkaline environment, its degradation ability is greatly inhibited. When a large amount of H^+ exists in the solution, the situation is just the opposite. It can transfer the photogenerated electrons to itself, which is further conducive to the generation of oxidizing hydroxyl radical and improve the degradation performance of the photocatalyst. Therefore, in the acidic range, the degradation performance of the catalyst is very good, and the degradation rate of the simulated dye RhB is also high.

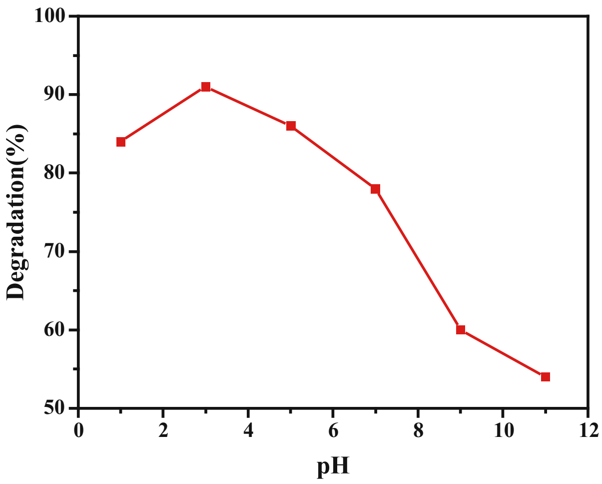

Figure 1: Effect of different pH solutions on the degradation performance of RhB.

3.2 Field emission scanning electron microscopy (FESEM) (ZG)

The morphology of the nanoparticles can be directly observed by FESEM. Figure 2a and b shows that the morphology of ZnO nanoparticles shows a relatively regular granular structure and all particles have a relatively uniform size, so the preparation of the material is successful. As can be seen in Figure 2c, the prepared samples have a lamellar structure that is mostly broken, with a highly irregular surface and the appearance of holes, probably because of the unsatisfactory melamine condensation effect during firing. The structure of the lamellae was thin and relatively uniformly distributed. Figure 2d–f presents the SEM scans of ZnO-g-C_3N_4 with different mass percentages of doped g-C_3N_4; it can be seen that the surface morphology of the binary composite ZnO-g-C_3N_4 is also small particles and shows a uniform distribution, in which g-C_3N_4 is not clearly visible in the figure, indicating that ZnO is dispersed more uniformly on the surface of the flake g-C_3N_4, which also indicates that the two materials have good affinity when they are compounded. Moreover, the microscopic morphology of g-C_3N_4-ZnO did not change significantly with the increase of the mass percentage of g-C_3N_4.

3.3 Transmission electron microscopy (TEM) (ZG)

To further observe the morphological characteristics inside the ZnO-g-C_3N_4 10% composite and the distribution of ZnO in g-C_3N_4, TEM characterization was performed. It can be seen from Figure 3a that ZnO is well dispersed, one by one in granular form with relatively uniform size. The spherical ZnO is attached to the g-C3N4 sheet in Figure 3b, verifying that the composite consists of ZnO and g-C_3N_4.

3.4 High-resolution transmission electron microscopy (HRTEM) (ZG QDs)

In order to obtain the morphological characteristics of ZnO QDs, HRTEM analysis was performed using the ZnO QDs. It can be seen that the produced samples are well dispersed

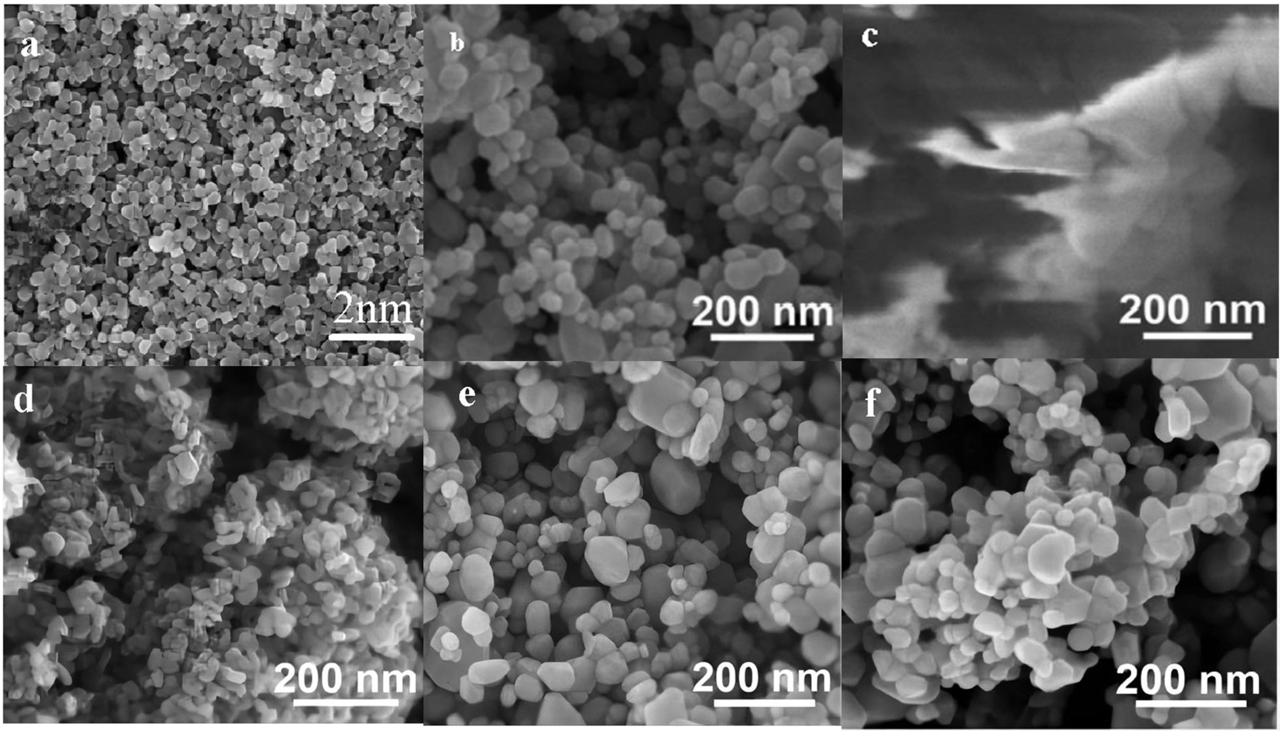

Figure 2: FESEM images of (a,b) ZnO, (c) g-C_3N_4, (d) ZnO-g-C_3N_4 3%, (e) ZnO-g-C_3N_4 10%, and (f) ZnO-g-C_3N_4 20% nanoparticles.

and have a relatively uniform particle size scale distribution. The dark-colored part with lattice display is the core of ZnO QDs. Figure 4a and b is the TEM image of ZnO QDs. As can be seen from the TEM image in Figure 4c, the sample prepared is the ZnO QDs-g-C_3N_4 composite structure.

3.5 X-ray diffractometry (XRD)

Figure 5 shows the XRD plots of ZnO-g-C_3N_4 binary composites with different g-C_3N_4 contents. And it can be seen that the XRD plots of ZC binary composites with different g-C_3N_4 contents correspond well with the XRD peak positions of single ZnO. The peak of g-C_3N_4 appeared at 2θ of 27.8° in the binary composites 20% ZC and 10% ZC, indicating that g-C_3N_4 was successfully compounded with ZnO by hydrothermal method. g-C_3N_4 peaks did not appear in the XRD plots of 3% ZC, 5% ZC, and 7% ZC, probably due to the relatively low content of g-C_3N_4. 10% ZC had the sharpest peak pattern with more prominent and better recognizability.

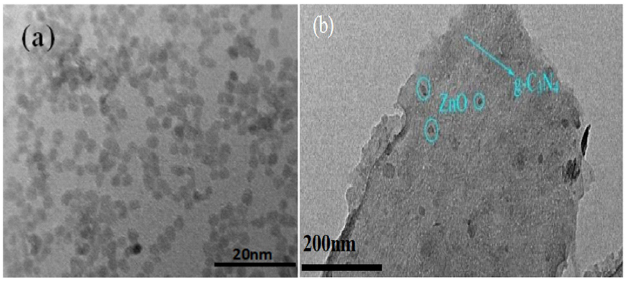

Figure 3: TEM diagram of (a) ZnO and (b) ZnO-g-C_3N_4 10% nanoparticles.

The data of the XRD patterns of ZnO QDs-g-C_3N_4 10%, ZnO-g-C_3N_4 10%, ZnO, and ZnO QD composite samples are displayed in Figure 6. It can be seen from the figure that compound ZnO QDs-g-C_3N_4 10% was compared with ZnO-g-C_3N_4 10%, and the peak area widened, which could improve the photocatalytic performance.

3.6 Fourier transform infrared (FT-IR)

The complexes also have typical stretching vibrational absorption peaks of g-C_3N_4 around 1240–1640 cm^{-1} and 810 cm^{-1}. This also indicates the successful complexation of ZnO, ZnO QDs with g-C_3N_4 in the complexes ZnO-g-C_3N_4 10%, ZnO QDs-g-C_3N_4 10%. The absorption peaks near 1,240–1,640 cm^{-1} and 810 cm^{-1} are attributed to the typical stretching vibration of g-C_3N_4, which also indicates the successful compounding of ZnO with g-C_3N_4 in the complex ZnO-g-C_3N_4.

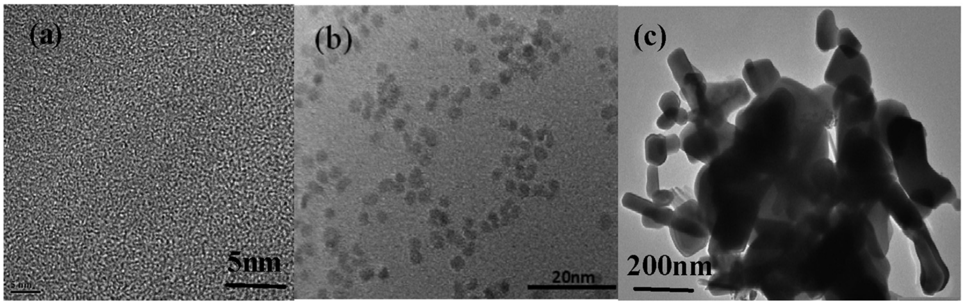

Figure 4: HRTEM images of (a,b) ZnO QDS and (c) ZnO QDS-g-C3N4 10% nanoparticles.

For the composites ZnO-g-C_3N_4 10%, ZnO QDs-g-C_3N_4 10%, it can be seen from Figure 8 that both have a wider typical absorption peak of ZnO in the range of 500 cm^{-1} vibrated by Zn-O stretching. The complexes also have typical stretching vibrational absorption peaks of g-C_3N_4 around 1240–1640 cm^{-1} and 810 cm^{-1}. This also indicates the successful complexation of ZnO, ZnO QDs with g-C_3N_4 in the complexes ZnO-g-C_3N_4 10%, ZnO QDs-g-C_3N_4 10% in the successful complexation of ZnO, ZnO QDs, and g-C_3N_4.

3.7 X-ray photoelectron spectroscopy (XPS)

Figure 9a–f presents the full spectrum analysis diagram of ZC QD composite sample and the XPS diagram of four elements. The presence of the four elements can be seen in the spectrogram of the XPS of the ZnOC QD composite in Figure 9a. The peak positions of C, N, O, and Zn in the binary composite can be determined from the figure, and there are no miscellaneous peaks in the figure, indicating the successful synthesis of ZC binary composite.

Figure 9b shows that C1s has three feature peaks. C1s peak with peak position of 284.6 eV is used in the experiment to achieve calibration of peak position error. The C1s orbital in ZC sample can be divided into C–C, C–O, and N–C═N components, whose binding energies are located at 284.8, 286.4, and 288.7 eV, respectively [52,53]. There are two peaks at 284.8 and 288.7 eV, which correspond to C–C and N–C═N groups in g-C_3N_4.

Figure 9c shows that O1s has three feature peaks, namely Zn–O, C═O/–OH, and C–O, with binding energies at 530.3, 531.8, and 533.0 eV, respectively. The XPS spectra of O1s of ZC were obtained at high resolution. Through Gaussian fitting, O with two components of binding energies of 530.3 and 531.4 eV was found. The peak of 531.4 eV binding energy is generally considered to be OH^- adsorbed on the surface of the material, and the peak of 530.3 eV is O^{2-} in ZnO [54–56].

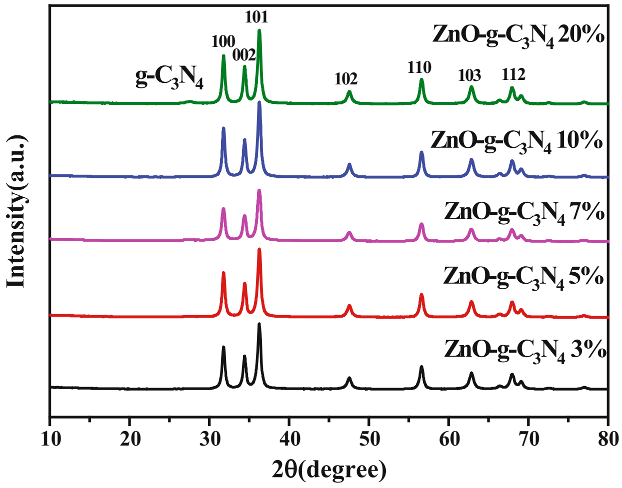

Figure 5: XRD diagram of composite samples with different g-C_3N_4 contents of ZnO-g-C_3N_4.

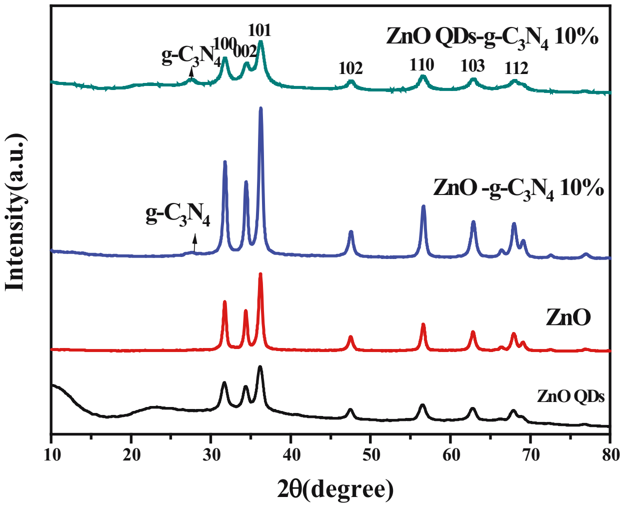

Figure 6: XRD plots of ZnOQDs-g-C_3N_4 10%, ZnO-g-C_3N_4 10%, ZnO, and ZnO QD composite samples.

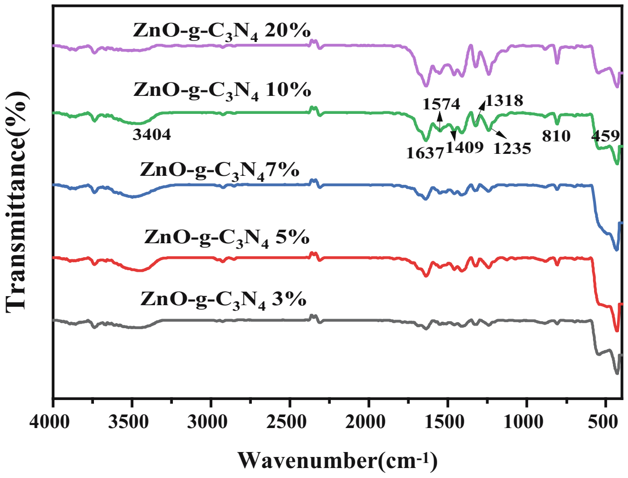

Figure 7: FT-IR spectrum map of the composite samples with different g-C_3N_4 contents of ZnO-g-C_3N_4.

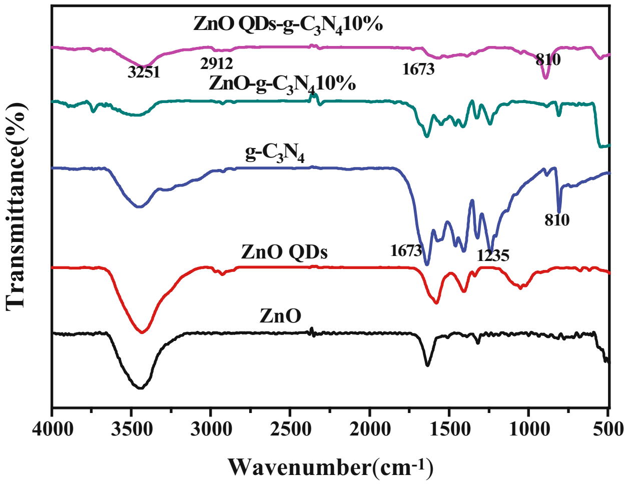

Figure 8: The FT-IR spectral map of ZnO-g-C_3N_4 10% and ZnO QDs-g-C_3N_4 10%.

As shown in Figure 9d and e, it can be seen that the energy difference of orbital spin splitting peaks ($2p^{3/2}$ and $2p^{1/2}$) in Zn2p spectrum is about 23 eV, and two peaks ($Zn2p^{3/2}$ and $2p^{1/2}$) appear at 1,021.7 and 1,044.8 eV, respectively, which is consistent with the XPS results of Zn^{2+} [57].

In Figure 9f, the 398.5 eV peak in N1s corresponds to the SP^2 hybrid aromatic bonded to carbon atoms in g-C_3N_4, and the corresponding 399.8 eV peak tertiary N(N–$(C)_3$/H–N–$(C)_2$); the third peak with high binding energy at 400.9 eV is attributed to quaternary N in an aromatic ring [54,58]. Through element analysis, this is consistent with the data in the existing literature. It further proves that the ZC QD composite sample is successfully prepared.

3.8 Diffuse reflectance spectroscopy

The pure ZnO and ZnO QDs are white, and when combined with g-C_3N_4, the color of the sample changes from white to light yellow. Pure ZnO and ZnO QDs show strong intrinsic absorption in UV region. At the same time, due to the presence of surface defects (such as Zni, VZn, and VO), ZnO and ZnO QDs also show a certain light response in the visible region. Figure 10 shows the UV spectra of g-C_3N_4 with different contents of ZnO-g-C_3N_4. g-C_3N_4 has a band edge positioned at about 460 nm, corresponding to a band gap of 2.70 eV. However, the visible light absorption of bulk g-C_3N_4 is weak in the visible region from 500 to 800 nm. Compared with pure ZnO, the absorption edge of the ZnO-g-C_3N_4 nanocomposite photocatalyst is red-shifted with the increase of g-C_3N_4 content in the feedstock and the visible light absorption becomes stronger. It is noteworthy that the best visible light absorption is achieved when the mass proportion of g-C_3N_4 is 10%. The visible light absorption of the composite photocatalyst decreased as the amount of g-C_3N_4 continued to increase, probably because the excess coverage of the amorphous g-C_3N_4 layer on the ZnO surface affected the light absorption rate.

According to Figure 11, the non-complex radiation centers are reduced, and the exciton absorption capacity is improved. ZnO QDs-g-C_3N_4 10% exciton absorption peak position and half peak width did not change significantly, indicating that the main body of the sample optical absorption is still ZnO core. The position of the 10% exciton absorption region of ZnO QDs-g-C_3N_4 has a slight red shift, because the particle size of QDs is changed due to the reaction conditions. In summary, ZnO QDs-g-C_3N_4 10% nanocomposite has the best photocatalytic performance.

3.9 Photoluminescence (PL)

The recombination of photogenerated electron-hole pairs causes luminescence (PL); therefore, measuring the intensity of PL spectra helps us further understand the transport and compounding processes of photogenerated carriers in semiconductors. The emission of PL is caused by the recombination of photogenerated carriers [59]. In general, the weaker the fluorescence intensity, the better the photocatalytic activity. It can be seen from Figure 12 that ZnO-g-C_3N_4 10% photocatalytic effect is the best. The PL intensity is significantly reduced due to the carrier transfer between valence band (VB) of g-C_3N_4 and conduction band (CB) of ZnO, which inhibits, and limits, the recombination of photogenerated carriers [60,61].

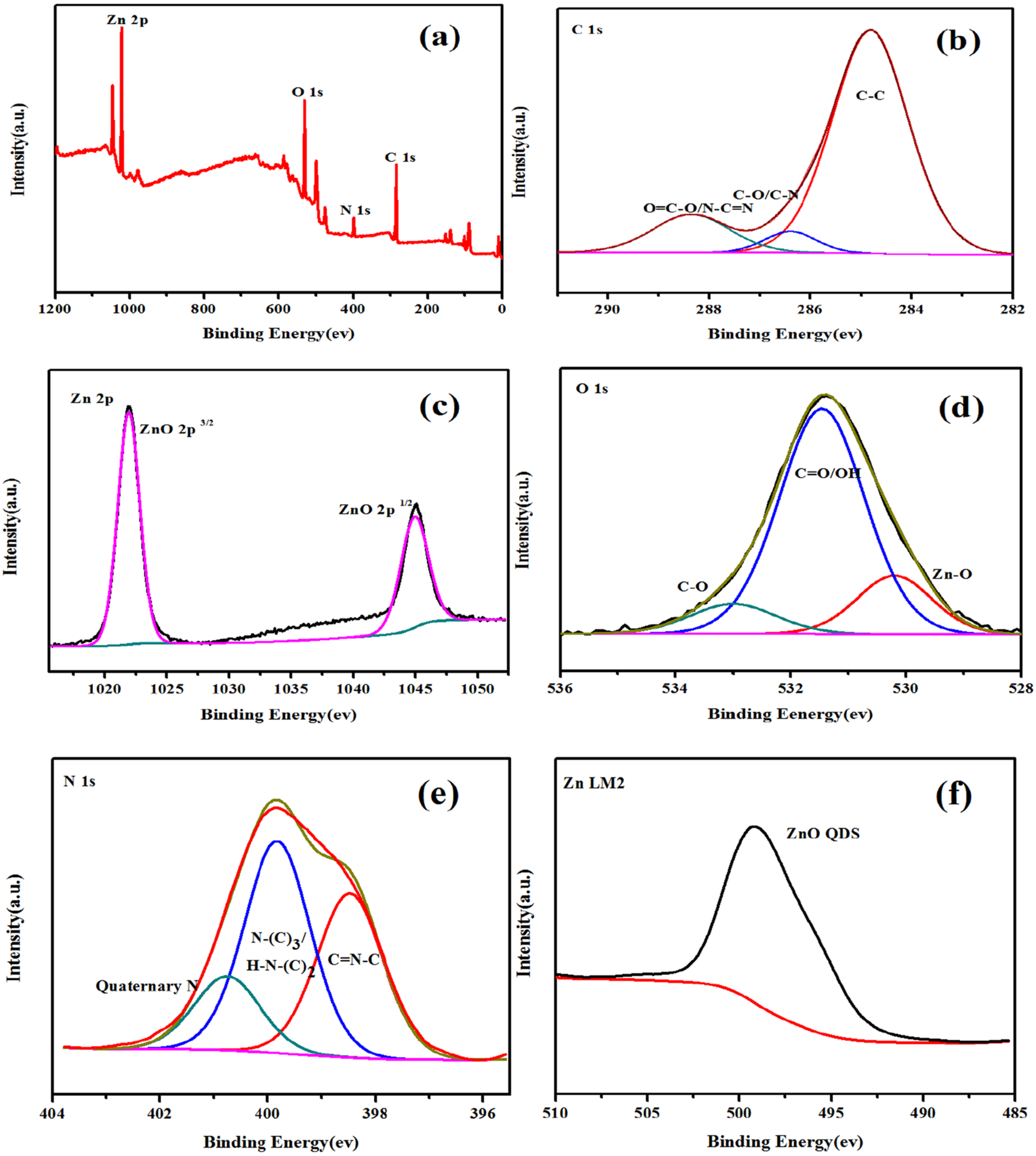

Figure 9: The full-spectrum analysis diagram of the ZC composite samples and the XPS diagram of the four elements. (a) Full spectrum of ZC composite sample, (b) C spectrum, (c) 2p spectrum of Zn, (d) O spectrum, (e) N spectrum, (f) LM2 spectrum of Zn.

3.10 Photocatalytic performance of different g-C_3N_4 doping amount catalysts

The experimental conditions are as follows: 10 mg·L^{-1} RhB solution 50 mL, photocatalyst ZnO-g-C_3N_4 dosage 0.02 g, pH = 3, room temperature, dark adsorption for 60 min, and light reaction time 6 h.

Figure 13 shows the degradation curves of catalysts with different g-C_3N_4 doping levels. The photocatalytic efficiency of RhB solution was investigated by using ZnO and g-C_3N_4 ZC binary composite materials with different doping mass ratios (3%, 5%, 7%, 10%, 20%) under visible light. Efficiency of photocatalytic degradation of composite materials with different g-C_3N_4 doping mass ratios was investigated by comparing with single ZnO.

As shown in Figure 13, the degradation rates of ZnO, ZC-3%, ZC-5%, ZC-7%, ZC-10%, and ZC-20% on RhB solution were 37.69%, 50.49%, 68.57%, 89.08%, 89.08%, and 80.96%, respectively, when visible light was irradiated for 360 min. It can be seen that in binary composite ZC, the higher the amount of g-C_3N_4 doping, the stronger the photocatalytic efficiency, and the visible light catalytic efficiency of ZC-10%

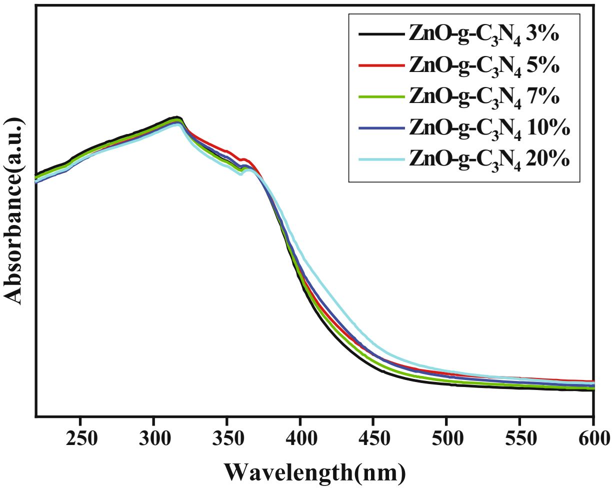

Figure 10: UV spectrogram of g-C_3N_4 with different contents of ZnO-g-C_3N_4.

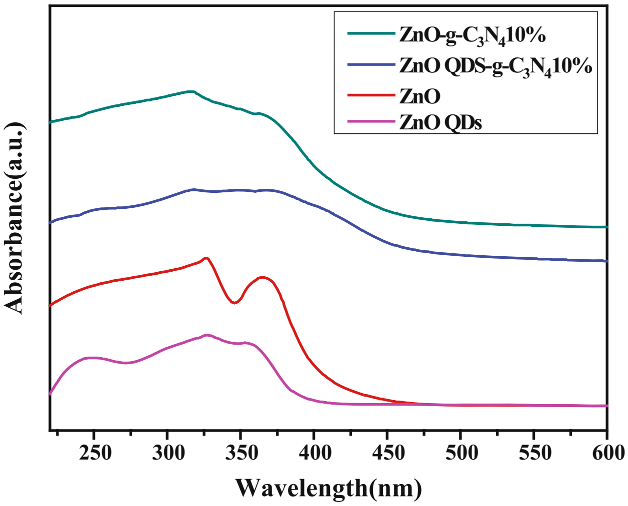

Figure 11: UV spectroscopy of ZnOQDs-g-C_3N_4 10%, ZnO-g-C_3N_4 10%, ZnOQDs, and ZnO.

is the highest. The main mechanism involves electron excitation from the VB of g-C_3N_4 to the CB under visible light irradiation, and then further transfer to the CB of ZnO. According to the aforementioned data, visible light catalytic efficiency is the best when the percentage of g-C_3N_4 is 10% in a certain range.

3.11 Photocatalytic activity of the optimum doping amount ZnO QDs-g-C_3N_4 catalyst

In the experiment, the photocatalytic ZnO-g-C_3N_4 10% degradation rate is the highest. Using ZnO-g-C_3N_4 10% as a reference to prepare the same proportion of ZnO QDs-g-C_3N_4 10% catalyst, its photocatalytic performance was explored. The experimental conditions are as follows: 50 mL, 10 mg·L^{-1} RhB solution, photocatalyst ZnO QDs-g-C_3N_4 0.02 g, pH = 3, room temperature, dark adsorption for 6 min, and light reaction time for 6 h.

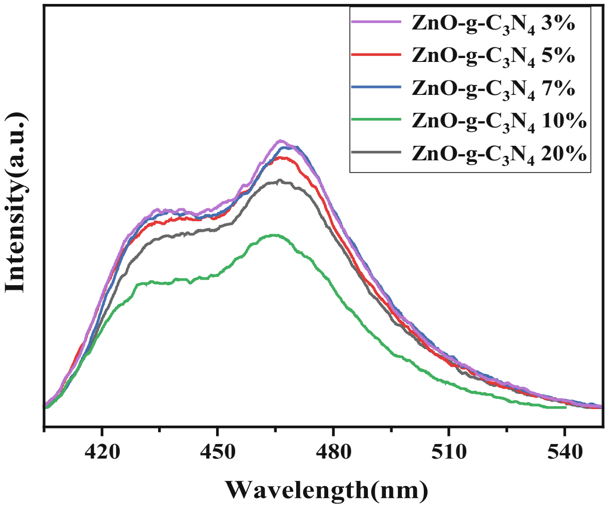

Figure 12: PL spectra of ZnO-g-C_3N_4 with different g-C_3N_4 contents.

Figure 14 is the degradation curve of ZnO QDs-g-C_3N_4 catalyst with the optimal doping amount. The graph shows that the adsorption energy of the photocatalyst doped with g-C_3N_4 was significantly enhanced during the dark adsorption process for the first 60 min. After 60 min, the degradation ability of the ZnO QDs-g-C_3N_4 composite photocatalyst doped with 10% g-C_3N_4 was significantly stronger than that of the pure ZnO-g-C_3N_4 powder catalyst.

When the light was turned on for 6 h, the degradation rate of pure ZnO was only about 33%, while that of the ZnO-

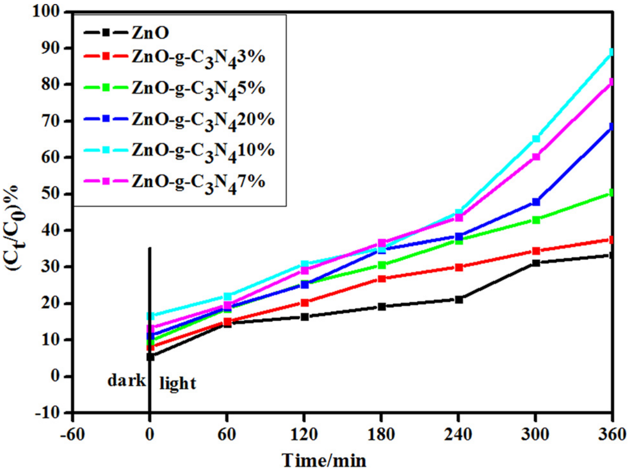

Figure 13: Degradation plots of different g-C_3N_4 doping catalysts.

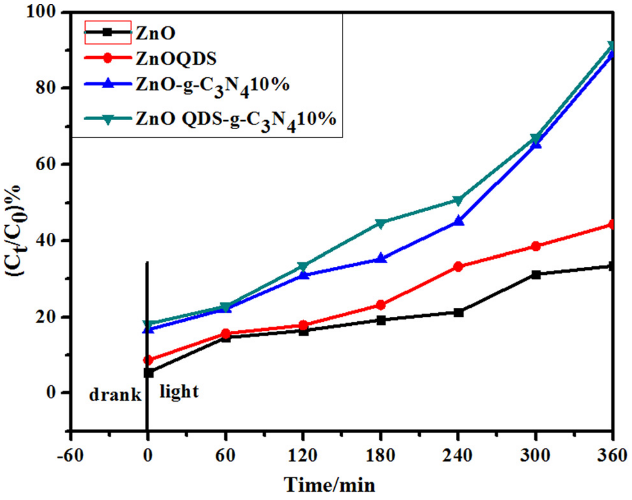

Figure 14: Degradation graph of optimal ZnOQDs-g-C_3N_4 catalyst.

g-C_3N_4 composite photocatalyst achieved almost 89% degradation. Compared with ZnO-g-C_3N_4 10%, ZnO QDs-g-C_3N_4 10% composite has smaller particle size, which increases the visible light absorption contact area and improves the photocatalytic efficiency. The photocatalytic efficiency of ZnO QDs-g-C_3N_4 10% composite was about 91%; it is obvious that the photo-catalytic efficiency of ZnO QDs-g-C_3N_4 10% was higher.

3.12 Photocatalytic reaction kinetics analysis of different g-C_3N_4 doping amount catalysts

To reach the adsorption–desorption equilibrium, the composite samples were subjected to a dark reaction in RhB for 1 h. Subsequent photodegradation was performed, and it can be seen from Figure 15 that the addition of g-C_3N_4 to form a binary hetero-junction improved the degradation efficiency of RhB.

The highest degradation efficiency was observed when the g-C_3N_4 doping was 10%, which may be related to the low efficiency of photo-generated electron-hole pair separation in the binary composite. It can be seen from Figure 15 that the photodegradation efficiency conforms to the first-order kinetic equation $\ln(C_t/C_o) = -kt$, where t and k represent the time constant and the rate constant, respectively.

As shown in Table 1, ZC-10% has a higher k value, $k = 0.002965$, which is about twice that of ZnO. R^2 of each ZC sample is more than 0.9, and it is concluded that each sample conforms to the first-order reaction kinetic equation for D_{RhB}.

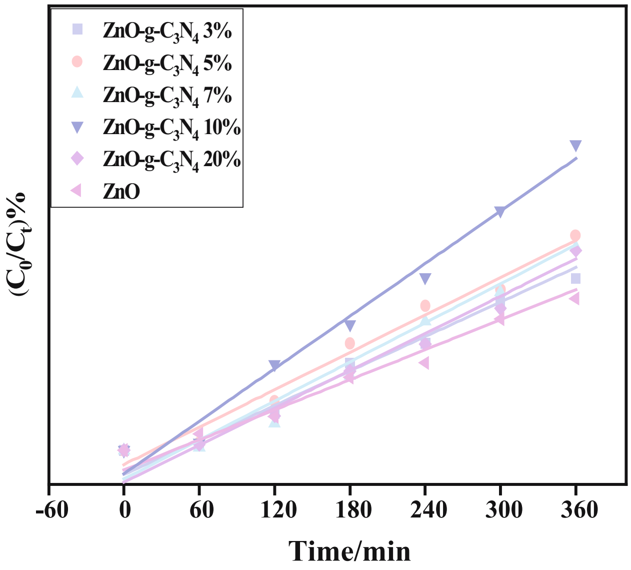

Figure 15: ZC photocatalytic degradation of RhB primary reaction kinetic constants.

3.13 Photocatalytic reaction kinetic analysis of optimum doping amount of ZnO-g-C_3N_4 and ZnO QDs-g-C_3N_4 catalysts

The starting time of the photoreaction was set to zero, and the $\ln(C_0/C_t)$ versus time t was analyzed for the ZC and ZC QD samples; as shown in Figure 16, a linear relationship exists for both samples, which is consistent with the primary reaction kinetics.

As shown in Table 2, ZC QDs-10% has the highest catalytic efficiency compared to other material, $k = 0.00323\ \text{min}^{-1}$, about 2.2 times that of ZnO nanotubes. The correlation coefficient R^2 of ZC QD composite sample is more than 0.9, and it is concluded that the sample conforms to the first-order reaction kinetic equation for D_{RhB}.

3.14 Cycle stability analysis

The stability and reusability of the catalysts were evaluated by cycling experiments of photocatalytic degradation of

Table 1: ZC photocatalytic degradation of RhB primary kinetic data

Sample name	Regression equation	*K*	R^2
ZnO	$y = 0.0995x - 0.1077$	0.00147	0.928
ZnO-g-C_3N_4 3%	$y = 0.1151x - 0.1327$	0.00168	0.9746
ZnO-g-C_3N_4 5%	$y = 0.1177x - 0.0781$	0.00182	0.9821
ZnO-g-C_3N_4 7%	$y = 0.1311x - 0.1575$	0.00190	0.9843
ZnO-g-C_3N_4 10%	$y = 0.1998x - 0.2098$	0.00296	0.9169
ZnO-g-C_3N_4 20%	$y = 0.1295x - 0.2182$	0.00182	0.8533

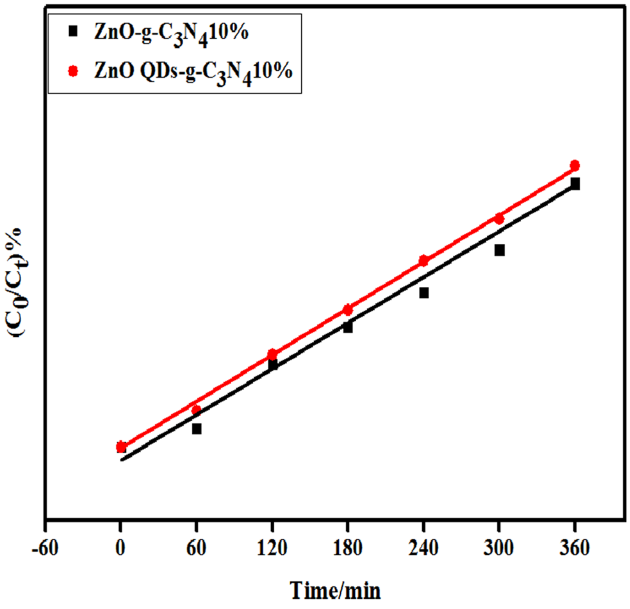

Figure 16: Primary reaction constant for the photocatalyzed degradation of RhB in composite samples with optimal doped amounts of g-C_3N_4.

RhB. The ZG-10% sample with the best photocatalytic performance was selected to be washed with water and alcohol four times, dried, sonicated, and dried, respectively, for recycling. The control light time was at 180 min, and five replicate experiments were conducted, and the results are shown in Figure 17.

It can be found that after repeating the experiment five times, the first degradation effect is the best, and after that the degradation rate decreases each time, but the change is not significant, and the catalyst still has a high degradation rate of about 83%. It showed that the catalysts were stable, regenerable, and reusable.

The 10% sample of ZnO QDs-g-C_3N_4 with the best photocatalytic performance was selected, filtered, sonicated, and dried, and then recovered for reuse. After repeating the experiment four times, the best degradation effect was achieved in the first time, and the degradation rate decreased in each subsequent time, but the change was not significant, and the catalyst still had a high degradation rate of about 85%. It showed that the catalysts were stable, regenerable, and reusable.

As can be seen from Figure 18, the photocatalytic degradation rate of the ZC QDs-10% photocatalyst decreased

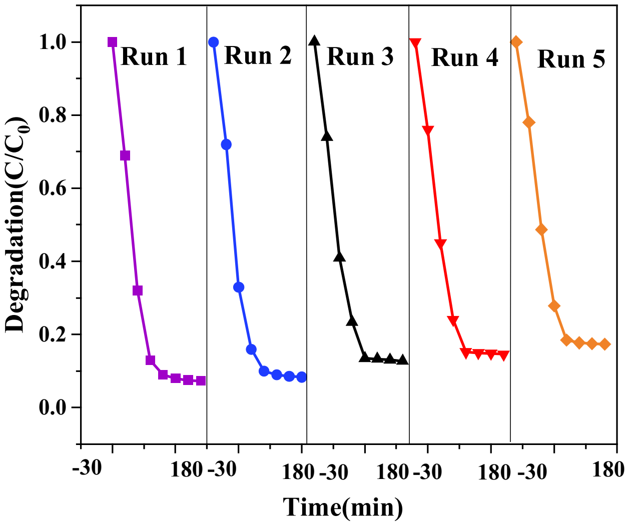

Figure 17: Stability of ZnO-g-C_3N_4 10% photocatalytic degradation of RhB.

somewhat after four uses, but the decrease was not significant, which may be due to the photocorrosion phenomenon of ZnO QDs. Overall, the prepared photocatalysts have good photocatalytic stability and repeated use performance.

3.15 Analysis of free radical capture experiment results

In order to elucidate the photocatalytic mechanism of ZC QD composite samples in more depth, different trapping agents were added in the photocatalytic process to identify

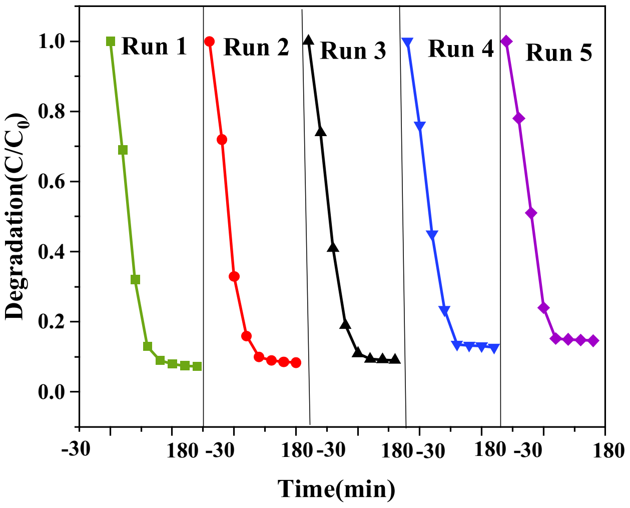

Figure 18: Stability of ZnO QDs-g-C_3N_4 10% photocatalytic degradation of RhB.

Table 2: Linear fit data for g-C_3N_4 optimal amount of composite material

Sample name	Regression equation	K	R^2
ZnO-g-C_3N_4 10%	$y = 0.1998x - 0.2098$	0.00296	0.9169
ZnO QDs-g-C_3N_4 10%	$y = 0.2174x - 0.2182$	0.00323	0.9525

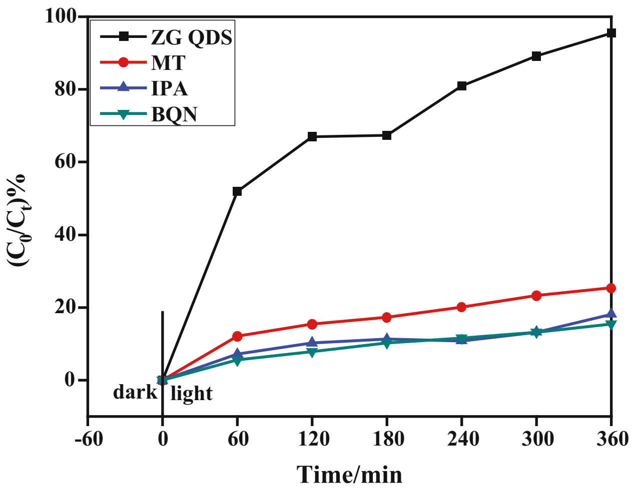

Figure 19: Photocatalytic performance of RhB by ZCQDs with BQN, MT, and IPA.

the main active species. The photocatalytic activity was significantly reduced after the addition of the trapping agents, indicating that the active species is the main active species under this photocatalytic system. ZC-10% was selected as a control for RhB degradation, and the changes in photocatalytic degradation of RhB after the addition of the three trapping agents and the results are shown in Figure 19.

As shown in Figure 19, the ZC QD sample D_{RhB} = 91.53%. To reveal the main active species in the photocatalytic degradation of RhB in ZC QD composites, *p*-benzoquinone (BQN), isopropyl alcohol (IPA), and methanol (MT) were added as superoxide radical ($^{\cdot}O^{2-}$), hydroxyl radical ($^{\cdot}OH$), and hole (h^+) trapping agents. The photocatalytic degradation efficiency of the samples showed a significant decrease when all three trapping agents were added, which indicated that $^{\cdot}O^{2-}$, $\cdot{}^{\cdot}OH$, and h^+ were the main active species in the photocatalytic process of the samples under visible light irradiation, where the effect size was $^{\cdot}O^{2-} > {}^{\cdot}OH > h^+$ in order.

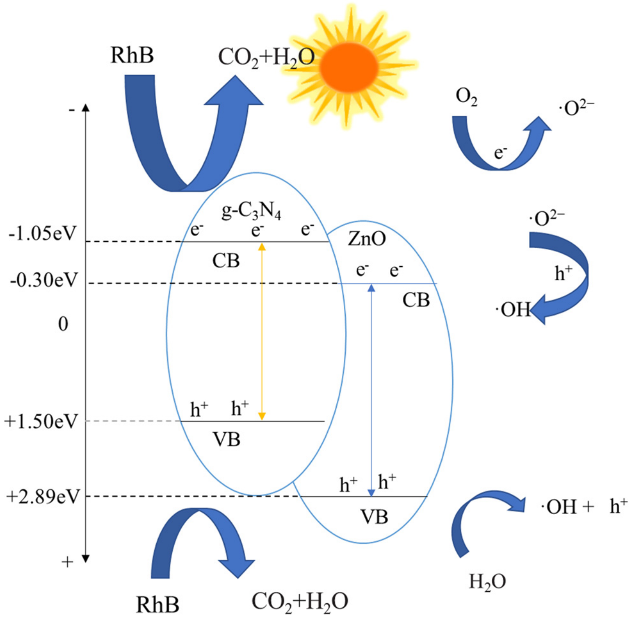

Figure 20: Schematic diagram of the photocatalytic reaction mechanism.

3.16 ZnO QDs-g-C_3N_4 10% catalyst mechanistic analysis

Under UV irradiation, g-C_3N_4 is excited to produce photogenerated electrons and holes. Because the CB of g-C_3N_4 is higher than that of ZnO, the generated photogenerated electrons are rapidly transferred from CB of g-C_3N_4 to CB of ZnO, which effectively prevents the electron-hole pair recombination. At the same time, the electrons in ZnO CB can reduce O_2 to form $^{\cdot}O^{2-}$, while the holes in g-C_3N_4 VB can combine with water to form $^{\cdot}OH$. RhB can also be directly oxidized to CO_2 and H_2O, thus degrading organic pollutants efficiently. The photocatalytic mechanism diagram is shown in Figure 20.

$$g\text{-}C_3N_4/ZnO + h\nu \rightarrow g\text{-}C_3N_4(e^-)/ZnO(e^-) + g\text{-}C_3N_4(h^+)/ZnO(e^-) \quad (1)$$

$$h^+ + H_2O \rightarrow ({}^{\cdot}OH) + h^+ \quad (2)$$

$$e^- + O_2 \rightarrow ({}^{\cdot}O_2) \quad (3)$$

$$({}^{\cdot}O_2) + 2h^+ \rightarrow 2({}^{\cdot}OH) \quad (4)$$

$$RhB + h^+/(({}^{\cdot}O_2{}^-)/({}^{\cdot}OH)) \rightarrow CO_2 + H_2O + \text{other molecules} \quad (5)$$

4 Conclusion

In this article, a series of ZnO-g-C_3N_4 composites, ZnO QDs-g-C_3N_4 composite photocatalysts, were prepared. The degradation ability of the catalysts for RhB pollutants was tested, and it was found that ZnO-g-C_3N_4 10% worked best. ZnO-g-C_3N_4 10% and ZnO QDs-g-C_3N_4 degradation rates under visible light conditions were 89.08% and 91.53%, respectively. The ability of the catalysts to degrade RhB pollutants was tested, and the cyclic stability of the catalysts and the photocatalytic mechanism of the active components of the composite samples were analyzed. Therefore, this work is helpful to enrich the preparation method of heterojunction and promote the further development of environmental wastewater purification research.

Funding information: This work was supported by the Natural Science Foundation of Heilongjiang Province (Grants No. LH2019H055), 2019 Heilongjiang University of Chinese Medicine “Outstanding Young Backbone Teachers Support Program” project, and Science and Technology Plan of Heilongjiang Provincial Health Commission (Grant No. 20222121 020963).

Author contributions: Haiyang Liu and Zhe Wang: writing – original draft preparation, writing – review and editing, methodology, formal analysis; Heng Zhang and Lixia Jin: writing – original draft preparation, formal analysis, visualization, project administration; Haiyang Liu: data analysis; Lixia Jin: resources. All authors have read and agreed to the published version of the manuscript.

Conflict of interest: The authors state no conflict of interest.

References

[1] Zhang C, Li Y, Shuai DM, Shen Y, Xiong W, Wang LQ. Graphitic carbon nitride (g-C$_3$N$_4$)-based photocatalysts for water disinfection and microbial control: A review. Chemosphere. 2019;214:462–79.

[2] Vattikuti SVP, Reddy PAK, Shim J, Byon C. Visible-light-driven photocatalytic activity of SnO$_2$–ZnO quantum dots anchored on g-C$_3$N$_4$ nanosheets for photocatalytic pollutant degradation and H$_2$ production. ACS Omega. 2018;3(7):7587–602.

[3] Jo WK, Selvam NCS. Enhanced visible light-driven photocatalytic performance of ZnO-g-C$_3$N$_4$ coupled with graphene oxide as a novel ternary nanocomposite. J Haz Mater. 2015;299:462–70.

[4] Amani-Ghadim AR, Arefi-Oskoui S, Mahmoudi R, Sareshkeh AT, Khataee A, Khodam F, et al. Improving photocatalytic activity of the ZnS QDs via lanthanide doping and photosensitizing with GO and g-C$_3$N$_4$ for degradation of an azo dye and bisphenol-A under visible light irradiation. Chemosphere. 2022;295:133917.

[5] Liu Y. Preparation method of g-C$_3$N$_4$ composite photocatalyst and its photo- catalytic performance. North China University of Science and Technology; 2021.

[6] Hashem EM, Hamza MA, Elshazly A, Elrahman SA, Elanany EM, Mohamed RT, et al. Novel Z-Scheme/Type-II CdS@ZnO/g-C$_3$N$_4$ ternary nanocomposites for the durable photodegradation of organics: Kinetic and mechanistic insights. Chemosphere. 2020;277:128730.

[7] Liu XL, Ma R, Zhuang L, Hu BW, Chen JR, Liu XY, et al. Recent developments of doped g-C$_3$N$_4$ photocatalysts for the degradation of organic pollutants. Crit Rev Env Sci Tec. 2021;51(8):751–90.

[8] Raaja Rajeshwari M, Kokilavani S, Sudheer, Khan S. Recent developments inarchitecturing the g-C$_3$N$_4$ based nanostructured photocatalysts: Synthesis, modifications and applications in water treatment. Chemosphere. 2022;291:132735.

[9] Zuarez-Chamba M, Rajendran S, Herrera-Robledo M, Priya AK, Navas-Cárdenas C. Bi-based photocatalysts for bacterial inactivation in water: Inactivation mechanisms, challenges, and strategies to improve the photocatalytic activity. Environ Res. 2022;209:112834.

[10] Cheng J, Yan X, Mo Q, Liu B, Wang J, Yang X, et al. Facile synthesis of g-C$_3$N$_4$/BiVO$_4$ heterojunctions with enhanced visible light photocatalytic performance. Ceram Int. 2017;43(1):301–7.

[11] Li J, Li Y, Zhang W, Naraginti S, Sivakumar A, Zhang C. Fabrication of novel tetrahedral Ag$_3$PO$_4$/g-C$_3$N$_4$/BiVO$_4$ ternary composite for efficient detoxification of sulfamethoxazole. Process Saf Environ. 2020;143:340–7.

[12] Hu J, Chen C, Zheng Y, Zhang G, Guo C, Li C. Spatially separating redox centers on Z-Scheme ZnIn2S4/BiVO$_4$ hierarchical heterostructure for highly efficient photocatalytic hydrogen evolution. Small. 2020;16(37):2002988.

[13] Ismael M. A review on graphitic carbon nitride (g-C$_3$N$_4$) based nanocomposites: Synthesis, categories, and their application in photocatalysis. J Alloy Compd. 2020;846:156446.

[14] Saha A, Chakraborti S. Effect of ZnO quantum dots on Escherichia coli global transcription regulator: A molecular investigation. Int J Biol Macromol. 2018;117:1280–8.

[15] Wu JM, Tsay LY. ZnO quantum dots-decorated ZnO nanowires for the enhancement of antibacterial and photocatalytic performances. Nanotechnology. 2015;26(39):395704.

[16] Sharma Y, Shubhangani S, Vineet S. Classification and impact of synthetic textile dyes on aquatic flora: a review. Reg Stud Mar Sci. 2021;45:101802.

[17] Benson NU, Agboola OD, Fred-Ahmadu OH, De-la-Torre GE, Oluwalana A, Williams AB. Micro(nano)plastics prevalence, food web interactions, and toxicity assessment in aquatic organisms: a review. Front in Mar Sci. 2022;9:851281.

[18] He Y, Wang Y, Hu J, Wang K, Zhai Y, Chen Y, et al. Photocatalytic property correlated with microstructural evolution of the biochar/ZnO composites. J Mater Res Technol. 2021;11:1308–21.

[19] Xue H, Wang X, Xu Q, Dhaouadi F, Sellaoui L, Seliem M, et al. Adsorption of methylene blue from aqueous solution on activated carbons and composite prepared from an agricultural waste biomass: A comparative study by experimental and advanced modeling analysis. Chem Eng J. 2022;430:132801.

[20] Sumanta S, Souman P, Sujata T, Satish K, Abhijit B, Uttam K, et al. Adsorption of methylene blue on chemically modified lychee seed biochar: dynamic, equilibrium, and thermodynamic study. J Mol Liq. 2020;315:113743.

[21] Hien TD, Nam TT, Dai XT. Investigation into the adsorption of methylene blue and methyl orange by UiO-66-NO$_2$ nanoparticles. J Anal Methods Chem. 2021;2021:5512174.

[22] Guo X, Han S, Yang J, Wang X, Chen S, Quan S. Effect of synergistic interplay between surface charge, crystalline defects, and pore volume of MIL-100(Fe) on adsorption of aqueous organic dyes. Ind Eng Chem Res. 2020;59:2113–22.

[23] Zhang Y, Han H, Wang X, Zhang M, Chen Y, Zhai C, et al. Utilization of NaP zeolite synthesized with different silicon species and NaAlO$_2$ from coal fly ash for the adsorption of rhodamine B. J Haz Mat. 2021;415:125627.

[24] Collins MC, Gunst PR, Cascio WE, Kypson AP, Muller-Borer BJ. Labeling and imaging mesenchymal stem cells with quantum dots. Methods Mol Biol. 2012;906:199–210.

[25] Xu J, Teslaa T, Wu TH, Chiou PY, Teitell MA, Teitell S. Nanoblade delivery and incorporation of quantum dot conjugates into tubulin networks in live cells. Nano Lett. 2012;12(11):5669–72.

[26] Chen G, Zhu JY, Zhang ZL, Zhang W, Ren JG, Wu M, et al. Transformation of cell-derived microparticles into quantum- dot-labeled nanovectors for antitumor siRNA delivery*Angew*. Chem Int (Edition in English). 2015;54(3):1036–40.

[27] Probst CE, Zrazhevskiy P, Bagalkot V, Gao X. Quantum dots as a platform for nanoparticle drug delivery vehicle design. Adv Drug Deliver Rev. 2013;65(5):703–18.

[28] Yong KT, Wang Y, Roy I, Rui H, Swihart MT, Law WC, et al. Preparation of quantum dot/drug nanoparticle formulations for traceable targeted delivery and therapy. Theranostics. 2012;2(7):681–94.

[29] Isherwood B, Timpson P, McGhee EJ, Anderson KI, Canel M, Serrels A, et al. Live cell in vitro and in vivo imaging applications: accelerating drug discovery. Pharmaceutics. 2011;3(2):141–70.

[30] Zamaleeva AI, Despras G, Luccardini C, Collot M, Waard M, Oheim M, et al. FRET-based nanobiosensors for imaging intracellular Ca^{2+} and H^+ Microdomains. Sensors (Basel). 2015;15(9):24662–80.

[31] Lan CX, Liu W, Cheng ZJ, Pan QS, Huang DS, Dong LX. Hydrothermal-based synthesis of CdS/ZnO quantum dots. Adv Mater Res. 2014;875–877:362–5.

[32] Liu KK, Shan CX, Zhou R, Zhao Q, Shen DZ. Large-scale synthesis of ZnO nanoparticles and their application as phosphors in light-emitting devices. Opt Mater Express. 2017;7(7):2682.

[33] Wang Y, Zhang X, Wang A, Li X, Wang G. Zhao. Synthesis of ZnO nanoparticles from microemulsions in a flow type microreactor. Chem Eng J. 2014;235:191–7.

[34] Nguyen HL. Reticular materials for artificial photoreduction of CO_2. Adv Energy Mater. 2020;46(10):200209.

[35] Song X, Li X, Zhang X. Fabricating C and O Co-doped carbon nitride with intramolecular donor-acceptor systems for efficient photoreduction of CO_2 to CO. Appl Catal B-Environ. 2020;268:118736.

[36] Mahvelati-Shamsabadi T, Lee BK. Photocatalytic H2 evolution and CO_2 reduction over phosphorus-doped g-C_3N_4 nanostructures: Electronic, optical, and surface properties. Renew Sust Energ Rev. 2020;130:109957.

[37] Jiang Z, Wan W, Li H, Yuan S, Zhao H, Wong P. A Hierarchical Z-scheme α-Fe_2O_3/g-C_3N_4 hybrid for enhanced photocatalytic CO_2 reduction. Adv Mater. 2018;30:1706108.

[38] Akhundi A, Habibi-Yangjeh A, Abitorabi M, Pouran S. Review on photocatalytic conversion of carbon dioxide to value-added compounds and renewable fuels by graphitic carbon nitride-based photocatalysts. Catal Rev. 2019;61:595–628.

[39] Sahua RS, Shiha Y, Chen WL. New insights of metal free 2D graphitic carbon nitride for photocatalytic degradation of bisphenol A. J Haz Mater. 2021;402:123509.

[40] Yang Y, Zeng G, Huang D, Zhang C, He D, Zhou C, et al. Molecular engineering of polymeric carbon nitride for highly efficient photocatalytic oxytetracycline degradation and H_2O_2 production. Appl Catal B-Environ. 2020;272:118970.

[41] Zhang Q, Peng Y, Lin Y, Wu S, Yu X, Yang C. Bisphenol S-doped g-C_3N_4 nanosheets modified by boron nitride quantum dots as efficient visible-light-driven photocatalysts for degradation of sulfamethazine. Chem Eng J. 2021;405:126661.

[42] Kurpil B, Markushyna Y, Savateev A. Visible-light-driven reductive (Cyclo) dimerization of chalcones over heterogeneous carbon nitride photocatalyst. ACS Catal. 2019;9:1531–8.

[43] Geng P, Tang Y, Pan G. A g-C_3N_4-based heterogeneous photocatalyst for visible light mediated aerobic benzylic C-H oxygenations. Green Chem. 2019;21:6116–22.

[44] Zhou Y, Zhang L, Wang W. Direct functionalization of methane into ethanol over copper modified polymeric carbon nitride via photocatalysis. Nat Commun. 2019;10:506.

[45] Hsu SH, Lin YY, Huang S, Lem KW, Nguyen DH, Lee DS. Synthesis of water-dispersible zinc oxide quantum dots with antibacterial activity and low cytotoxicity for cell labeling. Nanotechnology. 2013;24(47):475102.

[46] Thurston JH, Clifford AJ, Henderson BS, Smith TR, Quintana D, Cudworth KF, et al. Development of photoactive g-C_3N_4/Poly(vinyl alcohol) composite hydrogel films with antimicrobial and antibiofilm activity. ACS Appl Bio Mater. 2020;3(3):1681–9.

[47] Bellanger X, Billard P, Schneider R, Balan L, Merlin C. Stability and toxicity of ZnO quantum dots: Interplay between nanoparticles and bacteria. J Haz Mater. 2015;283:110–6.

[48] Mahmoodi NM, Karimi B, Mazarji M, Moghtaderi H. Cadmium selenide quantum dot-zinc oxide composite: Synthesis, characterization, dye removal ability with UV irradiation, and antibacterial activity as a safe and high-performance photocatalyst. J Photoch Photobio B. 2018;188:19–27.

[49] Waseem R, Syed MF, Mohammad O, Bahnemann D, Munee M. Facile fabrication of highly efficient modified ZnO photocatalyst with enhanced photocatalytic, antibacterial and anticancer activity. RSC Adv. 2016;6:78335–50.

[50] Suwiwat S, Andrew JH, Yuvarat N, Sujittra Y, Nontipa S. Rice straw-derived highly mesoporous carbon-zinc oxide nanocomposites as high performance photocatalytic adsorbents for toxic dyes. J Clean Prod. 2021;318:128583.

[51] Huang T, Chen J, Zhang L, Khataee A, Han Q, Liu X, et al. Precursor-modified strategy to synthesize thin porous amino-rich graphitic carbon nitride with enhanced photocatalytic de gradation of RhB and hydrogen evolution performances. Chin J Catal. 2022;43(22):497–506.

[52] Mishra DK, Mohapatra J, Sharma MK, Chattarjee R, Singh SK, Varma S, et al. Carbon doped ZnO: Synthesis, characterization and interpretation. J Magn Magn Mater. 2013;329:146–52.

[53] György E, Pérez Del Pino A, Logofatu C, Duta A, Isac L. Effect of nitrogen doping on wetting and photoactive properties of laser processed zinc oxide-graphene oxide nanocomposite layers. J Appl Phys. 2014;116:024906.

[54] Kumaresan N, Sinthiya MMA, Praveen Kumar M, Ravichandran S, Ramesh Babu R, Sethurman K, et al. Investigation on the g-C3N4 encapsulated ZnO nanorods heterojunction coupled with GO for effective photocatalytic activity under visible light irradiation. Arab J Chem. 2020;13:2826–43.

[55] Zhang X, Qin J, Hao R, Wang L, Shen X, Yu R, et al. Carbon-doped ZnO nanostructures: Facile synthesis and visible light photocatalytic applications. J Phys Chem C. 2015;119:20544–54.

[56] Dai K, Lu L, Liang C, Dai J, Zhu G, Liu Z, et al. Graphene oxide modified ZnO nanorods hybrid with high reusable photocatalytic activity under UV-LED irradiation. Mater Chem Phys. 2014;143:1410–6.

[57] de Moraes NP, Bacetto LA, dos Santos GS, Pinto da Silva MLC, Machado JPB, Campos TMB, et al. Synthesis of novel ZnO/carbon xerogel composites: Effect of carbon content and calcination temperature on their structural and photocatalytic properties. Ceram Int. 2019;45:3657–67.

[58] Zhu B, Xia P, Li Y, Ho W, Yu J. Fabrication and photocatalytic activity enhanced mechanism of direct Z-scheme g-C_3N_4/Ag_2WO_4 photocatalyst. Appl Surf Sci. 2017;391:175–83.

[59] Srinivas M. Preparation, characterization and photocatalytic activity of nickel-substituted $CoFe_2O_4$: exploration of changes in the micro structural parameters and distribution of cations in the lattice. Mater Res Express. 2019;6(11):1150f9.

[60] Prabhu S, Pudukudy M, Harish S, Navaneethan M, Sohila S, Murugesan K, et al. Facile construction of djembe-like ZnO and its composite with g-C_3N_4 as a visible-light-driven heterojunction photocatalyst for the degradation of organic dyes. Mater Sci Semicon Proc. 2020;106:104754.

[61] Guo X, Duan J, Li C, Zhang Z, Wang W. Highly efficient Z-scheme g-C_3N_4/ZnO photocatalysts constructed by co-melting-recrystallizing mixed precursors for wastewater treatment. J Mater Sci. 2020;55(5):2018–31.